Advanced Modeling and Simulation
in Engineering Sciences

RESEARCH ARTICLE　　　　　　　　　　　　　　　　　　**Open Access**

CrossMark

Displacement-based multiscale modeling of fiber-reinforced composites by means of proper orthogonal decomposition

Annika Radermacher[1], Brett A. Bednarcyk[2], Bertram Stier[1], Jaan Simon[1], Lei Zhou[1]
and Stefanie Reese[1*]

*Correspondence:
stefanie.reese@rwth-aachen.de
[1]Institute of Applied Mechanics,
Mies-van-der-Rohe-Str. 1, 52074
Aachen, Germany
Full list of author information is
available at the end of the article

Abstract

Many applications are based on the use of materials with heterogeneous microstructure. Prominent examples are fiber-reinforced composites, multi-phase steels or soft tissue to name only a few. The modeling of structures composed of such materials is suitably carried out at different scales. At the micro scale, the detailed microstructure is taken into account, whereas the modeling at the macro scale serves to include sophisticated structural geometries with complex boundary conditions. The procedure is crucially based on an intelligent bridging between the scales. One of the methods derived for this purpose is the meanwhile well established FE^2 method which, however, leads to a very high computational effort. Unfortunately, this impedes the use of the FE^2 method and similar methodologies for practically relevant problems as they occur e.g. in production or medical technology. The goal of the present paper is to significantly improve computational efficiency by using model reduction. The suggested procedure is very generally applicable. It holds for large deformations as well as for all relevant types of inelasticity. An important merit of the work is the computation of the consistent tangent operator based on the reduced stiffness matrix of the microstructure. In this way a very fast (in most cases quadratic) convergence within the Newton iteration at macro level is achieved.

Keywords: Proper orthogonal decomposition, Multiscale simulation, FE^2, Composites

Background

Many applications are based on the use of materials with heterogeneous microstructure. Prominent examples are fiber-reinforced composites, multi-phase steels or soft tissue to name only a few. The modeling of structures composed of such materials is suitably carried out at different scales. At the micro scale, the detailed microstructure is taken into account, whereas the modeling at the macro scale serves to include sophisticated structural geometries with complex boundary conditions. The procedure is crucially based on an intelligent bridging between the scales. This challenge, commonly denoted as multiscale modeling, has been in the center of international research for several years.

Among the methods which have been established for this purpose are the so-called FE^2 method (see e.g [1,2]) and the multiscale LATIN method (see e.g. [3,4]). A disadvantage

Springer Open

Radermacher *et al. Adv. Model. and Simul. in Eng. Sci.*(2016)3:29

Page 2 of 23

of the FE^2 method is the relatively high computational effort. The main reason for that is the fact that in every evaluation point of the macroscopic structure a boundary value problem has to be solved. This impedes the use of FE^2 for practically relevant problems as they occur e.g. in production or medical technology.

In the recent years, several methodologies have been developed to overcome this problem. One possibility is to take advantage of parallel computing e.g. like Feyel and Chaboche [1]. Another approach is to work with very efficient semi-analytical methods at the micro scale, for example, the generalized method of cells (GMC). This method has been developed, extended and widely used in the field of composites by Aboudi [5], Aboudi and Arnold [6]. In the GMC, the underlying repeating composite unit cell is discretized into sub-cells and the microscopic field equations of each sub-cell are explicitly coupled with the macroscopic constitutive equations without using finite elements. Michel and Suquet [7] embed the so-called nonuniform transformation field analysis (NTFA), introduced by the same authors in [8] and based on the early work of Dvorak and Benveniste [9], into a macroscopic finite element analysis for elastoplastic behavior with nonlinear isotropic hardening. The idea of the method is to create an effective constitutive relation for the nonlinear microstructure based on a reduced number of internal variables with inelastic modes to be defined by precomputed inelastic strain fields. The method is steadily further developed. Fritzen and Böhlke [10] show that the reduced basis order-reduction techniques applied in the NTFA can be very much improved by micromechanical considerations. Their method captures the anisotropic transient response of viscoelastic composites with a high gain in CPU time effort. Using a mixed variational framework, Fritzen and Leuschner [11] extend the previous concept to generalized standard materials. Further, consistency of the method is improved in the sense that an increasing number of basis functions leads to a monotonic increase of accuracy. In a very recent paper, Fritzen et al. [12] raise the speed-up of the method enormously by incorporating a parallel GPU implementation. The homogenization method of Fritzen and Leuschner [11] is additionally extended by nonuniform hardening modes which can account for locally varying hardening states. Largenton et al. [13] investigate several versions of the NTFA and apply their method to viscoelastic composites in the presence of aging and swelling. Another variant of the transformation field analysis is found in the paper of Oskay and Fish [14] and the follow-up work of Sparks and Oskay [15], where the evolution of failure is modeled by means of the eigen deformation.

Among the most common strategies to achieve model reduction in general are reduced basis (RB), proper orthogonal decomposition (POD) and proper generalized decomposition (PGD) techniques. Whereas the NTFA is either combined with RB, POD or mixtures of the two, there is a small group of authors who manage to incorporate the PGD into a multiscale framework. A good overview of the PGD is given by Chinesta et al. [16]. The procedure presented in Ladeveze et al. [17] is crucially based on the LATIN method which splits the entire problem into a macro problem defined over the whole structure and coarse sub-intervals which are treated along with linear micro problems. The PGD is applied on the latter which results into significant computational savings. In Ladeveze et al. [17] a viscoelastic fiber-reinforced structure is investigated. In a recent paper (Cremonesi et al. [18]), the method has been further refined by the derivation of the so-called homogenized operator and the extension of the PGD representation to the interface macro displacements. The, according to the knowledge of the authors, only combination of the FE^2

Radermacher *et al. Adv. Model. and Simul. in Eng. Sci.*(2016)3:29

Page 3 of 23

method with PGD is found in Halabi et al. [19], where a two-dimensional linear-elastic structure of simple geometry is investigated. Both the reduction in CPU time effort as well as the accuracy of the results show the high potential of this method.

One of the first papers on a "reduced" multiscale methodology involves the reduced-basis approach but is restricted to linear elasticity [20]. The very interesting question of error estimation has been investigated by Kerfriden et al. [21] in the context of projection-based reduced order modeling. By means of the derivation of upper and lower error bounds, the authors enable adaptive computations of random linear-elastic composites. The coupling of a reduced basis method to multiscale finite element methods for elliptic problems with highly oscillating coefficients can be found in Hesthaven et al. [22]. A finite element-based heterogeneous multiscale method applied to crack domains has been published in Abdulle and Bai [23].

Concerning nonlinear constitutive modeling, the work of Goury et al. [24] should be mentioned, where a FE^2 framework with damage is set up and the representative volume element (RVE) is modeled by POD. The investigation is restricted to a RVE with prescribed macroscopic strains. Highly interesting is the incorporation of the gappy method which allows to evaluate the internal force vector in only a small set of points of the structure. The selection of the points ("controlled" elements) is performed by means of the discrete empirical interpolation method. The example shows that—as expected—the maximum damage values are found between the inclusions. These are also the regions where the controlled elements are placed. A further development of the so-called gappy POD is found in the paper of Miled et al. [25] who couple the approach with the a priori hyperreduction method of Ryckelynck [26] to come to adaptive strategies for the computation of viscoelastic-viscoplastic composites. Closely related to hyperreduction is the method of empirical interpolation used by Hernandez et al. [27]. The latter authors apply POD at the level of their RVE which is assumed to behave elasto-plastically. An important merit of the paper is the development of a new interpolatory integration method which overcomes the well-known problem of ill-posedness when replacing the non-affine term only by POD terms. In the work of Monteiro et al. [28] nonlinearly electrical as well as nonlinearly thermal transient conduction problems are solved by means of a POD-reduced multiscale approach.

According to the knowledge of the authors there are hardly any contributions, where reduced multiscale modeling is applied to hyperelastic solids undergoing large deformation. In this context, it is important to mention the work of Yvonnet and He [29], who combine the FE^2 method with POD at the micro scale. The method shows very convincing results, whereby the reduction in CPU time effort leaves room for improvements. One reason for that could be the missing "analytical" (consistent) tangent which is replaced by a numerical tangent. Obviously, the computation of the latter is elaborate and leads to additional numerical effort. Very interesting is also the work of Xia and Breitkopf [30], where POD (at RVE level) and diffuse approximation techniques are combined to arrive at structural topology optimization of nonlinearly elastic structures. In order to cope with this challenging problem, the linearized strain measure is used throughout the paper.

The present work follows the line suggested by Yvonnet and He [29]. In the first part of the paper, the FE^2 method is presented in its standard format using periodic boundary conditions at the micro scale (not considered by Yvonnet and He [29]). The derivation incorporates large deformations, inelasticity as well as the formulation of the consistent

Radermacher *et al. Adv. Model. and Simul. in Eng. Sci.*(2016)3:29

Page 4 of 23

tangent to achieve approximately quadratic convergence in the Newton–Raphson iteration at the macro scale. In the second step, model reduction, more specifically POD, is brought into play which means to split the multiscale simulation into an offline and an online procedure. In the offline step, the so-called representative volume element or unit cell is subjected to nine characteristic deformation states additionally varied over time in order to compute a physically meaningful projection subspace. The latter is then used in the online step to significantly reduce the dimension of the equation system to be solved at the micro level. The work is crucially based on using the FE^2 interface of the finite element solver FEAP [31]. In this way, a very general multiscale solver is created. An important contribution of the work is the consistent tangent operator which is modified to incorporate the process of model reduction. The example computations performed in the third part of the paper show that speed-ups of two orders of magnitude can be reached. Very good results with negligible deviations from the reference simulation are achieved by means of only a small number of modes.

POD-based reduced multiscale method

Classical multiscale approach based on finite elements (FE^2)

Before presenting the reduced multiscale approach, attention is devoted to the classical first-order computational homogenization scheme. For detailed information please refer to e.g. Feyel [32], Kouznetsova [33], Miehe and Koch [34] and Geers et al. [2]. The local macroscopic constitutive response—for example given in terms of the first Piola-Kirchhoff stress tensor $\mathbf{P}_M$ in dependence of the macroscopic deformation gradient $\mathbf{F}_M$—is derived from the solution of a micro-structural boundary value problem in every evaluation point of the macroscopic structure. Speaking of FE^2 means that the spatial discretization at both scales is performed by means of finite elements. The volume to be considered at micro level should represent the usually heterogeneous microstructure sufficiently well. If this is the case, for a clear definition see the work of e.g. Kanit et al. [35], one speaks of a representative volume element (RVE). In the present work, we assume that a RVE is available. However, the present multiscale approach could be equally applied, if the conditions for the presence of a RVE were not fulfilled. Certainly then, the meaning of the results would have to be discussed with care.

In the following the three steps—macro-to-micro scale transition, solution of RVE boundary value problem, micro-to-macro scale transition—are briefly summarized.

Macro-to-micro scale transition

The macroscopic deformation gradient $\mathbf{F}_M$ which varies from point to point of the macroscopic structure is used to define the boundary conditions of the corresponding RVE problem:

$$\mathbf{x} = \mathbf{F}_M \, \mathbf{X} + \mathbf{w}. \tag{1}$$

In the latter relation (restricted to first order homogenization), $\mathbf{x}$ and $\mathbf{X}$ denote the position vectors of a material point in the current and the reference configuration, respectively. The vector $\mathbf{w}$ represents the so-called micro-fluctuation field imposed on the otherwise homogeneous deformation $\mathbf{F}_M \, \mathbf{X}$. The boundary conditions of the RVE can generally be derived from prescribed displacements, prescribed tractions or prescribed periodicity.

Radermacher *et al. Adv. Model. and Simul. in Eng. Sci.*(2016)3:29

Page 5 of 23

Periodic boundary conditions lead to more realistic modeling of the multiscale behavior which has been confirmed by several authors (see e.g. [36–38]). The periodicity conditions for the RVE are formulated as periodic displacements

$$\mathbf{u}^+ - \mathbf{u}^- = (\mathbf{F}_M - \mathbf{I})\,(\mathbf{X}^+ - \mathbf{X}^-) \tag{2}$$

and anti-periodic tractions

$$\mathbf{T}^+ = -\mathbf{T}^-. \tag{3}$$

The superscripts $+$ and $-$ correspond to opposite boundary surfaces ∂^+ and ∂^-. Using such boundary conditions the volume average theorem

$$\mathbf{F}_M = \frac{1}{V_0} \int_{V_0} \mathbf{F}_m \, dV_0 \tag{4}$$

for the microscopic deformation gradient $\mathbf{F}_m$ is automatically fulfilled (see e.g. [33] for a detailed derivation).

Solution of RVE boundary value problem

The RVE problem at the micro scale is a standard nonlinear quasi-static boundary value problem which requires to fulfill the balance of linear momentum

$$\operatorname{div} \mathbf{P}_{\mathrm{m}} = \mathbf{0}. \tag{5}$$

In the latter equation, dead load and inertia are neglected. Further, the tensor $\mathbf{P}_m$ represents the microscopic first Piola-Kirchhoff stress tensor. $\mathbf{P}_m$ is computed by means of the constitutive laws specifying the mechanical behavior for each micro-structural material constituent. FE^2 and also the reduced FE^2 approach presented in the next Section are in general applicable for arbitrary material laws. In the present paper, we concentrate ourselves on hyperelastic as well as elastoplastic material behavior. Thus, the stress tensor $\mathbf{P}_m$ is a function of the deformation gradient $\mathbf{F}_m$ as well as R internal variables $\mathbf{Q}_r$ (covering the elastoplastic behavior):

$$\mathbf{P}_m = \mathbf{f}\,(\mathbf{F}_m,\, \mathbf{Q}_r) \quad r \in [1, \dots, R]. \tag{6}$$

The internal variables are determined by evolution equations of type $\dot{\mathbf{Q}}_r = \mathbf{g}(\mathbf{F}_m,\, \mathbf{Q}_r)$ or $\dot{\mathbf{Q}}_r = \mathbf{g}(\mathbf{F}_m,\, \mathbf{Q}_r,\, \dot{\mathbf{Q}}_r)$ if rate-independent material behavior is considered.

Using a displacement-based finite element discretization, the following general nonlinear vector equation has to be solved:

$$\mathbf{G}(\bar{\mathbf{U}}) = \mathbf{R}(\bar{\mathbf{U}}) - \mathbf{L}\,(\bar{\mathbf{U}}) = \mathbf{0}. \tag{7}$$

In the latter relation, $\bar{\mathbf{U}}$ denotes the vector of all nodal displacements, $\mathbf{R}(\bar{\mathbf{U}})$ includes the internal forces and $\mathbf{L}\,(\bar{\mathbf{U}})$ the boundary forces. The boundary forces are here nodal reactions resulting from the prescribed displacement values at the boundary (periodic boundary conditions). It is assumed that the internal variables $\mathbf{Q}_r$ $(r = 1, \dots, R)$ are already determined at each Gauss point of the RVE. In this way, they can be seen as implicit functions of $\bar{\mathbf{U}}$ and do not show up as independent variables in (7).

Radermacher *et al. Adv. Model. and Simul. in Eng. Sci.*(2016)3:29

Page 6 of 23

The size of the equation system is the total number $\bar{n}$ of degrees-of-freedom of the RVE. The linearization of the nonlinear system (7) can be written as

$$\mathbf{G}(\bar{\mathbf{U}}^j) + \mathbf{K}^j \, \Delta \bar{\mathbf{U}}^{j+1} = \mathbf{0},$$
$$\bar{\mathbf{U}}^{j+1} = \bar{\mathbf{U}}^j + \Delta \bar{\mathbf{U}}^{j+1} \tag{8}$$

with the nonlinear stiffness matrix $\mathbf{K}^j = \partial \mathbf{G}/\partial \bar{\mathbf{U}}|_{\bar{\mathbf{U}}^j}$. In case of prescribed periodicity, the displacements of nodes on opposite RVE edges are assumed to be equal. For this reason, the nodal displacement vector $\bar{\mathbf{U}}$ is split into a part $\mathbf{U}_d$ which contains the n_d dependent degrees-of-freedom and a second part $\mathbf{U}_i$ where the n independent degrees-of-freedom are stored:

$$\bar{\mathbf{U}} = \begin{bmatrix} \mathbf{U}_d \\ \mathbf{U}_i \end{bmatrix}. \tag{9}$$

The two parts are connected by the constant matrix $\mathbf{C}$ leading to the relation $\mathbf{U}_d = \mathbf{C}\,\mathbf{U}_i$. Thus, the vector $\mathbf{U}_d$ can be eliminated from the system by means of condensation. One finally obtains the following linearized system for the n independent degrees-of-freedom included in $\mathbf{U}_i$:

$$\widetilde{\mathbf{G}}^j + \widetilde{\mathbf{K}}^j \, \Delta \mathbf{U}_i^{j+1} = \mathbf{0},$$
$$\mathbf{U}_i^{j+1} = \mathbf{U}_i^j + \Delta \mathbf{U}_i^{j+1}. \tag{10}$$

The $n \times n$ dimensional stiffness matrix $\widetilde{\mathbf{K}}^j$ is defined by $\widetilde{\mathbf{K}}^j = \mathbf{K}_{ii}^j + \mathbf{K}_{id}^j \, \mathbf{C} + \mathbf{C}^T \, \mathbf{K}_{di}^j + \mathbf{C}^T \, \mathbf{K}_{dd}^j \, \mathbf{C}$ and the $n \times 1$ vector $\widetilde{\mathbf{G}}^j$ by $\widetilde{\mathbf{G}}^j = \mathbf{G}_i(\bar{\mathbf{U}}^j) + \mathbf{C}^T \, \mathbf{G}_d(\bar{\mathbf{U}}^j)$, resulting from the decomposition (9). Note that $\mathbf{K}_{id}^j$ is the sub-matrix of $\mathbf{K}^j$ which contains the elements $(K^j)_{ab}$ with the indices a, b running according to $a = n_d + 1, \ldots, \bar{n}$ and $b = 1, \ldots, n_d$, respectively. The other quantities in the equations for $\widetilde{\mathbf{K}}^j$ and $\widetilde{\mathbf{G}}^j$ are determined analogously.

Furthermore, the displacement vector $\mathbf{U}_i$ is split into

$$\mathbf{U}_i = \begin{bmatrix} \mathbf{U}_b \\ \mathbf{U}_f \end{bmatrix}. \tag{11}$$

The $n_b \times 1$ vector $\mathbf{U}_b$ contains the prescribed nodal displacements at the specified boundary nodes, whereas the unknown nodal displacements of the remaining nodes are described by the $n_f \times 1$ vector $\mathbf{U}_f$. Note that the sum of n_b and n_f is equal to n ($n = n_b + n_f$). The linearization (10) including the decomposition of the displacement components into $\mathbf{U}_b$ and $\mathbf{U}_f$ (11) is written as

$$\underbrace{\begin{bmatrix} \mathbf{K}_{bb} & \mathbf{K}_{bf} \\ \mathbf{K}_{fb} & \mathbf{K}_{ff} \end{bmatrix}^j}_{\widetilde{\mathbf{K}}^j} \begin{bmatrix} \Delta \mathbf{U}_b \\ \Delta \mathbf{U}_f \end{bmatrix}^{j+1} = - \underbrace{\begin{bmatrix} \mathbf{G}_b \\ \mathbf{G}_f \end{bmatrix}^j}_{\widetilde{\mathbf{G}}^j}. \tag{12}$$

The displacements at the boundary are prescribed so that $\Delta \mathbf{U}_b$ vanishes in the iterative solution process. On the right hand side, $\mathbf{G}_f$ can be expressed by

$$\mathbf{G}_f = \mathbf{R}_f - \mathbf{L}_f, \tag{13}$$

Radermacher *et al. Adv. Model. and Simul. in Eng. Sci.*(2016)3:29

Page 7 of 23

where $\mathbf{L}_f$ is zero, because reaction forces only occur at the boundaries. Solving (12) for the unknown displacement vector $\mathbf{U}_f$ leads to the following iterative solution algorithm at the micro scale:

$$
\begin{aligned}
\mathbf{K}_{ff}^j \, \Delta \mathbf{U}_f^{j+1} &= -\mathbf{R}_f^j, \\
\mathbf{U}_f^{j+1} &= \mathbf{U}_f^j + \Delta \mathbf{U}_f^{j+1}, \\
||\mathbf{R}_f^{j+1}|| &\leq \text{tol}, \\
j &\leftarrow j+1.
\end{aligned}
\tag{14}
$$

Micro-to-macro scale transition

Upon the solution of the RVE problem, the macroscopic stress tensor $\mathbf{P}_M$ is obtained by computing the volume average of the micro-structural stress field $\mathbf{P}_m$. In addition, to achieve quadratic convergence at the macro level, the correct macroscopic tangent $\mathbf{C}_M$ in $\Delta \mathbf{P}_M = \mathbf{C}_M : \Delta \mathbf{F}_M$ is needed. Note that $\mathbf{C}_M$ includes in general geometric and material parts (see e.g. [39]).

For the derivation of the tangent the macroscopic stress tensor $\mathbf{P}_M$ is expressed as the volume average

$$
\mathbf{P}_M = \frac{1}{V_0} \int_{V_0} \mathbf{P}_m \, dV_0 = \frac{1}{V_0} \int_B \mathbf{T} \otimes \mathbf{X} \, dB
\tag{15}
$$

of the microscopic stress tensor $\mathbf{P}_m$, where $\mathbf{T}$ is the stress vector defined by Cauchy's lemma $\mathbf{T} = \mathbf{P}\,\mathbf{N}$ ($\mathbf{N}$ outward unit normal vector with respect to the surface of the reference configuration). Here, it is exploited that firstly the volume integral (15) can be reduced to a integral over the boundary B by using the divergence theorem and, secondly, that the divergence of $\mathbf{P}_m$ vanishes in the micro-structural equilibrium. For a detailed derivation of this step, we refer to Kouznetsova et al. [38] and Kouznetsova [33]. In the case of a finite element discretization of the RVE, the boundary integral in Eq. (15) is computed as sum of the products of the 3×1 nodal reaction vector $\mathbf{L}_b^A$ and the 3×1 position vector $\mathbf{X}^A$ at the N_b prescribed boundary nodes $A \in [1, N_b]$:

$$
(P_M)_{nm} = \frac{1}{V_0} \sum_{A=1}^{N_b} (L_b)_n^A \, X_m^A.
\tag{16}
$$

To extract the macroscopic tangent $\mathbf{C}_M$ based on the RVE solution, we follow the scheme presented by Kouznetsova [33] and Kouznetsova et al. [38]. Using the latter relation, we can state

$$
(\Delta P_M)_{nm} = \frac{1}{V_0} \sum_{A=1}^{N_b} (\Delta L_b)_n^A \, X_m^A.
\tag{17}
$$

The next task is to obtain $(\Delta L_b)_n^A$. At the end of the Newton iteration at the micro level, the relation $\mathbf{G}_f = \mathbf{0}$ holds. Thus, at this stage the increment $\Delta \mathbf{U}_f$ is simply given by

$$
\Delta \mathbf{U}_f = -\mathbf{K}_{ff}^{-1} \, \mathbf{K}_{fb} \, \Delta \mathbf{U}_b.
\tag{18}
$$

Further, $\mathbf{G}_b = \mathbf{0}$ must be fulfilled resulting into $\Delta \mathbf{G}_b = \Delta \mathbf{R}_b - \Delta \mathbf{L}_b = \mathbf{0}$ and consequently $\Delta \mathbf{L}_b = \Delta \mathbf{R}_b$. Exploiting (18) lets us finally write

$$\Delta \mathbf{L}_b = \Delta \mathbf{R}_b = (\mathbf{K}_{bb} - \mathbf{K}_{bf} \, \mathbf{K}_{ff}^{-1} \, \mathbf{K}_{fb}) \, \Delta \mathbf{U}_b = \mathbf{K}^{\star} \, \Delta \mathbf{U}_b, \tag{19}$$

where $\mathbf{K}^{\star}$ has the dimension $n_b \times n_b$. The latter equation provides a relation between $\Delta \mathbf{L}_b$ and $\Delta \mathbf{U}_b$. Due to periodicity, the increment $\Delta \mathbf{U}_b^B$ is given at each node B by the relation

$$\Delta \mathbf{U}_b^B = \Delta \mathbf{F}_M \, \mathbf{X}^B. \tag{20}$$

It remains to fill this information into (17) which leads to

$$\begin{aligned}
(\Delta P_M)_{nm} &= \frac{1}{V_0} \sum_{A=1}^{N_b} (\Delta L_b)_n^A \, X_m^A \\
&= \underbrace{\frac{1}{V_0} \sum_{A=1}^{N_b} \sum_{B=1}^{N_b} (K^{\star})_{nx}^{AB} \, X_m^A \, X_y^B}_{(C_M)_{nmxy}} \, (\Delta F_M)_{xy}.
\end{aligned} \tag{21}$$

Index notation is used for the sake of better readability. The summation over lower-case letters is defined by Einstein's summation convention. It should be emphasized that the presented FE^2 concept is generally valid for large strain inelasticity. The microscopic consistent tangent tensor $\mathbf{C}_m$ in $\Delta \mathbf{P}_m = \mathbf{C}_m : \Delta \mathbf{F}_m$ is hidden in the matrix $\mathbf{K}^{\star}$. Obviously, quadratic convergence at the macro level can only be achieved if $\mathbf{C}_m$ as well as $\mathbf{C}_M$ are correctly computed.

POD-based multiscale method (FEPOD)

The idea of the proposed POD-based multiscale approach is to couple a POD-reduced RVE simulation at the micro scale to a finite element computation (without any reduction) at the macro scale. Therefore, in each evaluation point of the macroscopic system, a *reduced* RVE computation is performed to define the current stress state instead of a standard finite element computation as in the classical approach.

The macro-to-micro scale transition as explained above can be used without any changes for the reduced approach. In contrast, the RVE problem as well as the macro-to-micro scale transition differ from the classical approach.

Solution of reduced RVE boundary value problem

The computation is split as usual into an offline and an online part, to apply POD-based model reduction at the micro scale. The offline part is used to define a suitable lower dimensional subspace. In the computationally efficient online step the reduced computation of the RVE based on this subspace is performed.

In the **offline step**, the RVE is analyzed for each independent deformation mode separately. In the case of small deformations, we use six precomputations: the three tension modes and the three shear modes. In the case of large deformations, nine precomputations are investigated corresponding to the nine entries in the deformation gradient $\mathbf{F}_M$. The subspace is computed by using the method of snapshots [40,41]. A snapshot is one computed solution vector $\mathbf{U}_f$ of a full-dimensional microstructural FE simulation. Obviously, for each precomputation, arbitrarily many snapshots can be stored. The choice of

Radermacher *et al. Adv. Model. and Simul. in Eng. Sci.*(2016)3:29

Page 9 of 23

the number of snapshots is very much dependent on the problem under investigation. In particular, the material behavior plays a major role. In the context of inelasticity, it becomes necessary to store snapshots on loading as well as on unloading paths. Also the time dependence of the material behavior is an aspect which deserves special attention.

If the number of snapshots is lower than their dimension (which is usually the case), the method of snapshots is very efficient to compute the lower-dimensional subspace. The l computed solution vectors $\mathbf{U}_f$ of the unknown displacement dofs in these evaluated full-field simulations according to Eq. (14) are saved in the $n_f \times l$-dimensional snapshot matrix $\mathbf{D} = [\mathbf{U}_f^1, \mathbf{U}_f^2, \cdots, \mathbf{U}_f^l]$. The computation of the lower-dimensional subspace is based on the minimization of the approximation error of the collected snapshots and their new approximation. In addition orthogonality is claimed. These conditions lead to an eigenvalue problem of the correlation matrix $1/l\ \mathbf{D}^T \mathbf{D}$. The $n_f \times m$ projection matrix $\mathbf{\Phi}$ is then filled with the m eigenvectors—multiplied by $\mathbf{D}$ and normalized—corresponding to the first m largest eigenvalues of the correlation matrix. The offline part has to be evaluated once for each type of RVE and has to be performed before the multiscale simulation.

In the **online step** of the multiscale simulation, the reduced RVE is called in each material point of the macroscopic system. Therefore, the unknown displacements of the RVE boundary value problem (14) are approximated by

$$\mathbf{U}_f = \mathbf{\Phi}\,\mathbf{U}_{red} \tag{22}$$

where $\mathbf{\Phi}$ is the $n_f \times m$-dimensional subspace matrix. In this way the n_f-dimensional displacement vector $\mathbf{U}_f$ is reduced to the m-dimensional unknown vector $\mathbf{U}_{red}$. Typically, the reduced dimension m is much smaller than the full dimension n_f: $m \ll n_f$.

Inserting the approximation (22) into the nonlinear boundary value problem of the RVE (14) and using a Galerkin projection, leads to the following iterative solution algorithm:

$$\underbrace{\mathbf{\Phi}^T \mathbf{K}_{ff}^j \mathbf{\Phi}}_{\mathbf{K}_{red}} \Delta\mathbf{U}_{red}^{j+1} = -\underbrace{\mathbf{\Phi}^T \mathbf{R}_f^j}_{\mathbf{R}_{red}},$$

$$\mathbf{U}_f^{j+1} = \mathbf{U}_f^j + \mathbf{\Phi}\Delta\mathbf{U}_{red}^{j+1},$$

$$||\mathbf{R}_{red}^{j+1}|| \le \text{tol},$$

$$j \leftarrow j + 1. \tag{23}$$

The dimension of the reduced equation system is m instead of the full dimension n_f, thus solving the RVE problem is computationally much more efficient than in the classical approach. In the case of nonlinear mechanical RVE problems, it is still necessary to evaluate all local quantities (stress and material tangent) in each evaluation point of the RVE (see for a more detailed derivation of the presently used POD method in the nonlinear context [42,43]). In order to reduce the computational effort further, extended projection-based reduction methods have been developed (e.g. [26,27,44–49]). The idea of such methods is in general to significantly reduce the number of evaluation points. This important step could be also integrated into the present method but goes beyond the scope of this paper.

Reduced micro-to-macro scale transition
To couple the reduced RVE computation with the finite element computation on the macro scale, we use the same ansatz as in the classical approach (see "Classical multiscale

Radermacher *et al. Adv. Model. and Simul. in Eng. Sci.*(2016)3:29

Page 10 of 23

approach based on finite elements (FE^2)" section). Since now a reduced RVE computation is used, the computation of the matrix $\mathbf{K}^\star$ differs from the classical approach. It is evident that eq. (18) (see "Classical multiscale approach based on finite elements (FE^2)" section) has to be replaced by

$$\Delta \mathbf{U}_{red} = -(\mathbf{K}_{red})^{-1} \, \boldsymbol{\Phi}^T \, \mathbf{K}_{fb} \, \Delta \mathbf{U}_b. \tag{24}$$

Since the relation $\Delta \mathbf{R}_b = \Delta \mathbf{L}_b$ remains, we only need to exploit that $\Delta \mathbf{R}_b$ reads in the reduced case

$$\Delta \mathbf{R}_b = \mathbf{K}_{bf} \, \boldsymbol{\Phi} \, \Delta \mathbf{U}_{red} + \mathbf{K}_{bb} \, \Delta \mathbf{U}_b. \tag{25}$$

Using Eq. (24) one arrives at

$$\Delta \mathbf{R}_b = (\mathbf{K}_{bb} - \mathbf{K}_{bf} \, \boldsymbol{\Phi} \, (\mathbf{K}_{red})^{-1} \, \boldsymbol{\Phi}^T \, \mathbf{K}_{fb}) \, \Delta \mathbf{U}_b = \mathbf{K}^\star \, \Delta \mathbf{U}_b. \tag{26}$$

With the matrix $\mathbf{K}^\star$ being determined in this way, the macroscopic tangent $\mathbf{C}_M = (C_M)_{ijkl} = \mathbf{e}_i \otimes \mathbf{e}_j \otimes \mathbf{e}_k \otimes \mathbf{e}_l$ can be computed exactly in the same way as before:

$$(C_M)_{ijkl} = \frac{1}{V_0} \sum_{A=1}^{N_b} \sum_{B=1}^{N_b} (K^\star)_{ik}^{AB} X_j^A X_l^B. \tag{27}$$

Summary of FEPOD

Table 1 summarizes the presented reduced multiscale approach. In the offline step, the RVE is analyzed for prescribed independent deformation modes separately. These are standard mechanical simulations of the microstructural boundary value problem. Based on the computed solutions (snapshots) the subspace $\boldsymbol{\Phi}$ is computed for the RVE. Afterwards, in the online step the multiscale simulation with reduction is done. Therefore, in a first step the macroscopic model has to be defined. The material behavior is defined by coupling RVEs to the macroscopic material constituents, which have to be initialized. Then the nonlinear mechanical simulation of the macroscopic model starts. A load increment is applied to the macroscopic structure and the nonlinear deformation response is computed in a Newton–Raphson scheme. Thereby, a nested reduced nonlinear FE simulation of the RVE problem is called in each integration point of the macroscopic model. The current macroscopic deformation gradient sets the boundary conditions for the current reduced RVE computation. The RVE problem is then calculated using POD reduction. If the RVE boundary value problem is converged, the macroscopic stress tensor as well as the material tangent are computed by means of averaging the microscopic data using the equations derived in the previous subsections. After the problem has converged on the macro scale the next load increment is applied.

Numerical results

Multiscale problem settings

To investigate the proposed multiscale approach, the following bending problem of a cantilever sheet is investigated. Geometry and boundary conditions are shown in Fig. 1. The sheet has the dimensions $240\,\text{mm} \times 120\,\text{mm} \times 0.1\,\text{mm}$ and is fixed at $x = 0\,\text{mm}$.

Table 1 Solution scheme of FEPOD

	Macroscale	Microscale
Offline		Set up RVE
		Apply predefined idenpendent deformation states
		Run and save solutions for each case
		Calculate subspace for each RVE separately
Online	1. Set up macroscopic model	
	Geometry, boundary conditions	Initialize RVEs
	FE discretization	Load subspace
	Set RVEs for each material	
	2. Run simulation	
	Loop time or load step	
	Apply load increment	
	Loop Newton iteration	
	Loop elements	
	Loop material points	
	Calculate $\mathbf{F}_M$	
	Load history variables	
	$\Rightarrow$	Calculate boundary conditions for RVE
		Solve RVE with POD reduction
		If convergence is reached:
		Calculate $\mathbf{P}_M$
		Calculate $\mathbf{C}_M$
		Save local history variables globally
	Store $\mathbf{P}_M$, $\mathbf{C}_M$ and history $\Leftarrow$	
	End (material points)	
	End (elements)	
	Global assembling	
	Check convergence	
	If converged: BREAK	
	End (Newton iteration)	
	Update displacements	
	End (time/load step)	

At $x = 240$ mm it is loaded by a prescribed displacement in y-direction. The macro model is discretized with $6 \times 3 \times 1$ elements leading to a number of 152 not constrained displacement degrees-of-freedom.

The underlying micro scale system, which will be active at each integration point in the macro scale sheet problem, is given in Fig. 2. A random arrangement of four fibers in a matrix is used (see [50]). The fiber volume fraction is 42.6% and the RVE measures $19 \times 19 \times 0.95$ mm^3. The RVE is discretized in all three dimensions and as such solved as a full 3D problem. In the third direction, 2 elements are used. The microscopic problem includes 3286 elements, 5088 nodes with 3 degrees-of-freedom and in total 9858 independent displacement degrees-of-freedom. In the following, an elastic composite as well as an elastoplastic metal matrix composite are investigated.
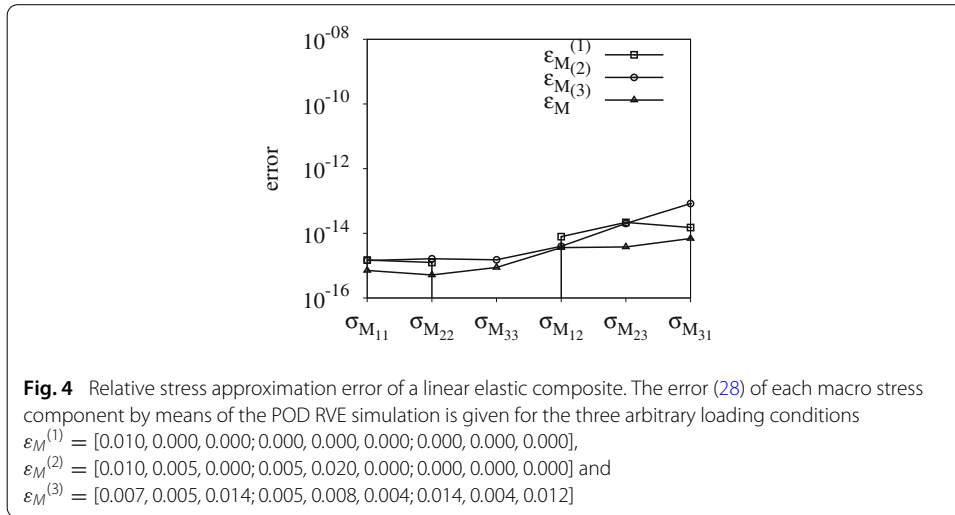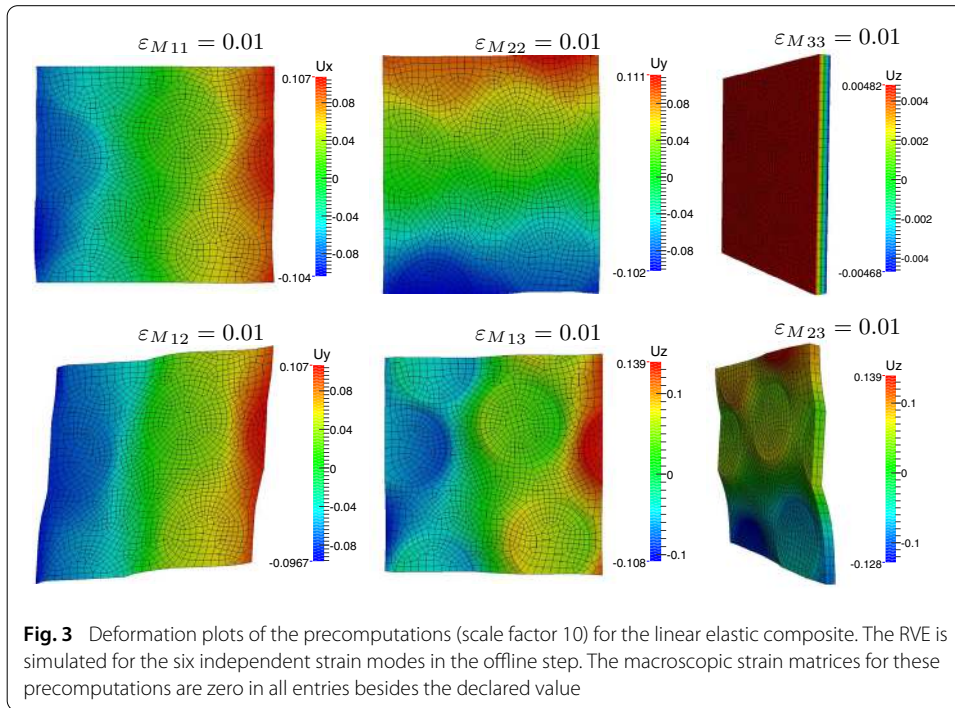
Linear elastic material behavior
To demonstrate the offline step and to validate the proposed approach of a POD-reduced RVE computation in the framework of FE^2 (FEPOD), first purely linear elastic material behavior is assumed for both, the fiber and matrix constituents. The matrix is modeled

Fig. 1 Geometry and boundary conditions of the bending test. A cantilever sheet with dimensions 240 mm × 120 mm × 0.1 mm is investigated

Fig. 2 RVE geometry. The RVE contains four randomly arranged fibers (*blue*) and the matrix (*red*). Dimensions are arbitrary
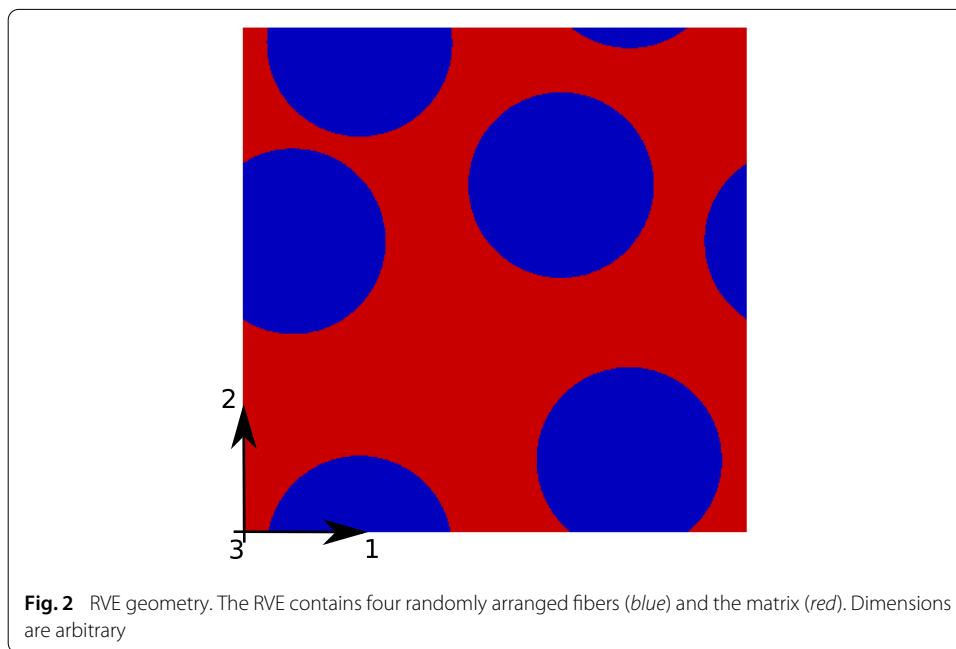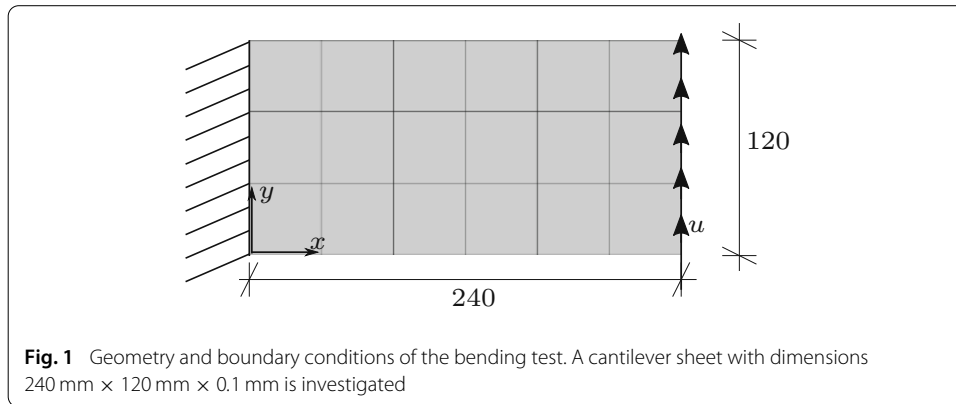
as isotropically elastic (Young's modulus $E_m = 3600\,\text{N/mm}^2$, Poisson's ratio $\nu_m = 0.38$). The contribution of the fibers is represented by orthotropic elasticity (Young's modulus parallel to the fibers $E_{\parallel} = 230000\,\text{N/mm}^2$, Young's modulus perpendicular to the fibers $E_{\perp} = 15000\,\text{N/mm}^2$, shear moduli $G_{\perp\parallel} = G_{\parallel\perp} = 15000\,\text{N/mm}^2$, Poisson's ratios $\nu_{\perp\perp} = 0.4$ and $\nu_{\parallel\perp} = 0.2$). These material parameters were determined experimentally (see [51]).

To compute the snapshots for the POD reduction of the RVE, the six independent strain states are investigated in the offline step. Deformations for each of the six applied strain modes are shown in Fig. 3. In each precomputation one displacement vector is collected and saved into the snapshot matrix **D**. From these six displacement vectors, six POD modes are computed. The eigenvalue problem of the correlation matrix results in six nonzero eigenvalues (eigenvalues range from 0.0025 to 1.65).

To investigate the accuracy of the POD-reduced RVE computation, we apply three arbitrary macroscopic loading conditions ε_M onto the RVE and compare the results with an unreduced RVE computation. Figure 4 shows the approximation error in the macroscopic stress response (Cauchy stress matrix σ_M) of a reduced RVE computation with six POD modes. The stress approximation error is computed by means of the relation

Fig. 3 Deformation plots of the precomputations (scale factor 10) for the linear elastic composite. The RVE is simulated for the six independent strain modes in the offline step. The macroscopic strain matrices for these precomputations are zero in all entries besides the declared value

Fig. 4 Relative stress approximation error of a linear elastic composite. The error (28) of each macro stress component by means of the POD RVE simulation is given for the three arbitrary loading conditions
$\varepsilon_M^{(1)} = [0.010, 0.000, 0.000; 0.000, 0.000, 0.000; 0.000, 0.000, 0.000]$,
$\varepsilon_M^{(2)} = [0.010, 0.005, 0.000; 0.005, 0.020, 0.000; 0.000, 0.000, 0.000]$ and
$\varepsilon_M^{(3)} = [0.007, 0.005, 0.014; 0.005, 0.008, 0.004; 0.014, 0.004, 0.012]$

$$\text{error } \sigma_{Mij} = \frac{|\overline{\sigma_M}_{ij} - \sigma_{Mij}|}{|\sigma_{Mij}|} \tag{28}$$

where $\overline{\sigma_M}_{ij}$ denotes the approximate solution of the POD computation and σ_{Mij} the solution of the unreduced simulation serving as reference solution. The indices i and j refer to the components of the matrix. As expected, the comparison shows a perfect agreement between the unreduced and the reduced solution (effectively zero approximation errors). Of course, this can only be reached in the case of linear elasticity where the principle of superposition holds. At the RVE scale, the POD simulation runs around 60 times faster than the unreduced simulation.

Table 2 Relative displacement and relative stress deviations of the multiscale problem with a linear elastic RVE

	u_x	u_y	u_z			
Min (error)	0	0	0			
Max (error)	0	0	$1.86 \cdot 10^{-8}$			
	σ_{xx}	σ_{yy}	σ_{zz}	σ_{xy}	σ_{yz}	σ_{zx}
Min (error)	0	0	$1.98 \cdot 10^{-14}$	0	$4.58 \cdot 10^{-9}$	$2.05 \cdot 10^{-8}$
Max (error)	$9.06 \cdot 10^{-10}$	$8.52 \cdot 10^{-10}$	$1.16 \cdot 10^{-9}$	$6.17 \cdot 10^{-10}$	$6.30 \cdot 10^{-5}$	$1.89 \cdot 10^{-3}$

The table gives the extreme values of the relative deviation $|\Delta(*)|^* = |\overline{(*)} - (*)|/\max(|(*)|)$ of each displacement component $\overline{u_i}$ and stress field $\overline{\sigma}_{ij}$ computed in the FEPOD computation in comparison with the corresponding values $(*)$ of the reference FE^2 computation for the multiscale example with linear elastic material behavior

The previous computation took place only at the micro scale. In the next step, the accuracy and computational efficiency of the reduced multiscale simulation is investigated. For this purpose, the macro model shown in Fig. 1, coupled with the reduced RVE computation discussed above, is investigated. As expected, the displacement as well as the stress deviations on the macro level summarized in Table 2 are vanishingly small. The relative stress deviations in the main directions $(x - y)$ are in the range of 10^{-10}. The higher deviations of the shear stresses concerning the third direction are located close to the clamped boundary. An enormous speed-up of 255 is reached. The linear multiscale problem converges in one step, as expected.

This first example shows the validity of the presented reduced multiscale approach, especially the computation of the consistent tangent based on the reduced stiffness matrix and its implementation in the FE^2 framework of the finite element solver FEAP [31], in the context of linear elasticity.

Elastoplastic material behavior

In the next step, we investigate a metal matrix composite. The matrix is modeled as elastoplastic material with a Young's modulus of $E = 110300 \, \text{N/mm}^2$ and a Poisson's ratio of $v = 0.26$. The yield stress is $\sigma_y = 371.5 \, \text{N/mm}^2$ and the linear hardening modulus is $H = 28921.5 \, \text{N/mm}^2$. The isotropic fibers behave linearly elastically with a Young's modulus of $E_f = 393000 \, \text{N/mm}^2$ and a Poisson' ratio of $v_f = 0.25$. The elastoplastic behavior of the microstructure is represented in Fig. 5. The stress-strain relation of the RVE for uniaxial loading in x-as well as in y-direction is shown. The curves show a pronounced hardening effect and a high degree of plastification.
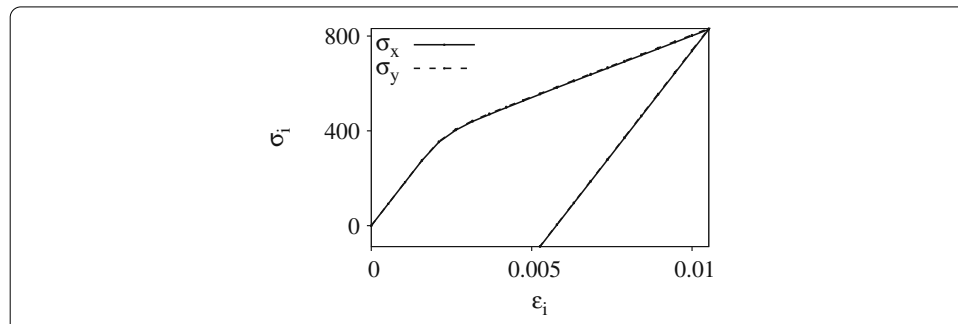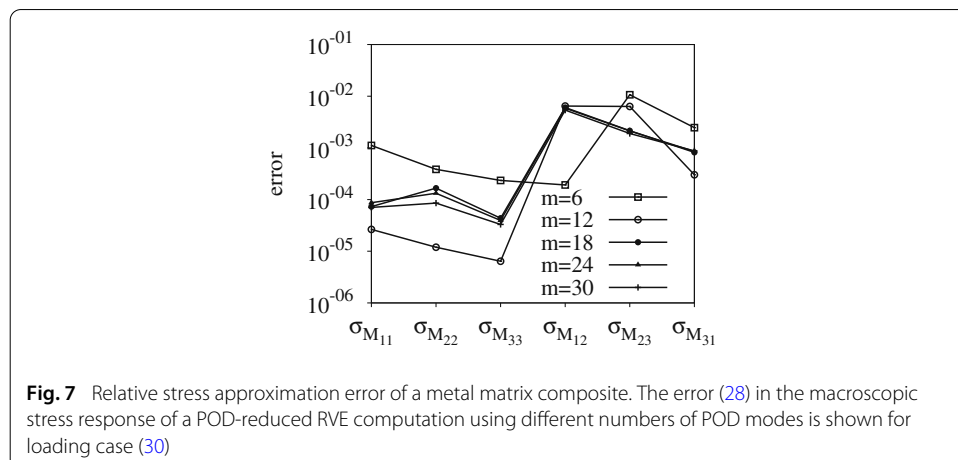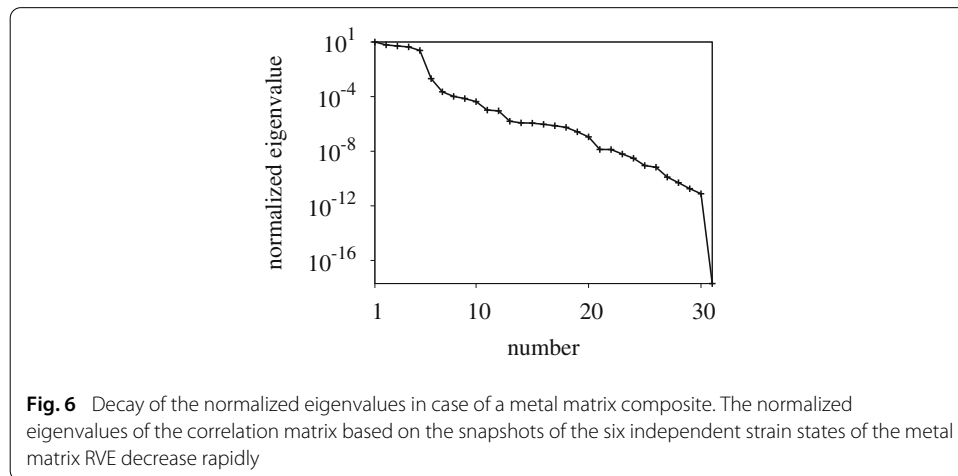

Fig. 5 Stress–strain relation of the metal matrix composite RVE. The plastic behavior of the microstructure is plotted based on uniaxial loading tests in x- and y-direction

Again, to compute the snapshots, the six independent strain states are simulated in the offline step. In order to account for the plastic behavior, in each precomputation, the strain state is applied over a time interval $t \in [0, 1]$ and five snapshots over the time interval are stored into the snapshot matrix $\mathbf{D}$. In this way, in total 30 snapshots are collected in the offline step. The POD modes are again computed from this data set by solving the above-mentioned eigenvalue problem of the correlation matrix. The decay of the eigenvalues is shown in Fig. 6. In contrast to the previous elastic example, the number of nonzero eigenvalues is larger than the six investigated independent strain states. Nevertheless, a rapid decay can be observed, which guarantees good results using the POD reduction.

Considering first the metal matrix composite RVE alone, Fig. 7 shows the approximation error (Eq. (28)) in the macroscopic stress response (Cauchy stresses) of a POD-reduced RVE computation using different numbers of POD modes. The RVE is arbitrarily loaded by the macroscopic strain state (given in matrix form)

$$
\varepsilon_M = \begin{bmatrix} 0.007 & 0.005 & 0.014 \\ 0.005 & 0.008 & 0.004 \\ 0.014 & 0.004 & 0.012 \end{bmatrix}.
$$
(29)

Fig. 6 Decay of the normalized eigenvalues in case of a metal matrix composite. The normalized eigenvalues of the correlation matrix based on the snapshots of the six independent strain states of the metal matrix RVE decrease rapidly

Fig. 7 Relative stress approximation error of a metal matrix composite. The error (28) in the macroscopic stress response of a POD-reduced RVE computation using different numbers of POD modes is shown for loading case (30)

As expected the errors are larger than in the previous purely elastic example. The error depends on the number of POD modes computed in the offline step. Using more than six POD modes leads to significantly smaller errors. In summary, a good accuracy with errors smaller than one per cent can be reached by using only 12 POD modes. This POD-reduced RVE computation with 12 POD modes runs around 220 times faster than the unreduced reference solution. Of course, the speed-up depends on the number of POD modes. It decreases from 260 to 60 by increasing the number of POD modes from 6 to 30.

In the next step, we focus on the multiscale simulation. In case of elastoplastic behavior, the macrostructural bending test described in the previous Section is investigated under loading as well as unloading. The influence of the number of POD modes for the RVE reduction is investigated. Tables 3 and 4 show the deviation of the displacement, the stress fields as well as the accumulated plastic strain field of a FEPOD simulation with 6, 12 and 24 POD modes with respect to a standard FE^2 simulation. Tables 3 compares the values at the end of the loading time and Table 4 the values at the end of the unloading time. The results of the FEPOD multiscale approach fit those of the reference FE^2 approach very well. Again, using more POD modes leads to better agreement with the reference results, but of course, also with a smaller speed-up. With 6 POD modes a speed-up of 225 can be reached. This speed-up falls to 165 by using 24 POD modes. The loading part is captured more precisely compared to the unloading part. This is due to the chosen RVE precomputations which do not explicitly include unloading. Nevertheless, relative deviations smaller than 5% are reached in the end of the multiscale simulation. At the point of maximum loading the relative deviations are in the range of 10^{-4}. Higher maximal deviations can be observed for the displacement in the third direction as well as the shear stresses concerning this direction. The main deformation of the example takes place in the $x - y$ plane so that the POD modes (concerning the highest eigenvalues) cover the main behavior as well as possible. In other directions the reduced system can lead to higher deviation, but the high error values occur only in a few points.

The comparison of the overall behavior is shown in the reaction force versus displacement plot in Fig. 8 as well as in the zoomed part of Fig. 9. The sum of the reaction forces is plotted against the prescribed displacement u_y. Again a very good agreement of the FEPOD results for 12 or more POD modes is shown. The FEPOD method can capture

Table 3 Relative displacement, accumulated plastic strain and stress deviations of the multiscale problem with a elastoplastic RVE for different numbers of POD modes at time point of maximum loading

	u_x	u_y	u_z	ε_{pl}		
$m = 6$	$2.8 \cdot 10^{-3}$	$5.5 \cdot 10^{-4}$	16.5	$4.8 \cdot 10^{-3}$		
$m = 12$	$5.0 \cdot 10^{-4}$	$1.6 \cdot 10^{-4}$	4.5	$7.0 \cdot 10^{-4}$		
$m = 24$	$1.5 \cdot 10^{-4}$	$4.5 \cdot 10^{-5}$	0.7	$1.5 \cdot 10^{-5}$		
	σ_{xx}	σ_{yy}	σ_{zz}	σ_{xy}	σ_{xz}	σ_{yz}
$m = 6$	$1.3 \cdot 10^{-2}$	$2.5 \cdot 10^{-3}$	$4.3 \cdot 10^{-3}$	$1.1 \cdot 10^{-2}$	12.8	1.0
$m = 12$	$1.9 \cdot 10^{-3}$	$7.4 \cdot 10^{-4}$	$9.5 \cdot 10^{-4}$	$2.4 \cdot 10^{-3}$	2.3	0.4
$m = 24$	$6.6 \cdot 10^{-5}$	$2.9 \cdot 10^{-4}$	$5.3 \cdot 10^{-5}$	$2.2 \cdot 10^{-4}$	0.15	0.19

The table gives the maximum values of the relative deviation $|\Delta(*)|^* = |\overline{(*)} - (*)|/max(|(*)|)$ of each field $\overline{(*)}$ computed in the FEPOD computation in comparison with the corresponding field $(*)$ of the reference FE^2 computation for the multiscale example with elastoplastic material behavior and a different number of POD modes

Table 4 Relative displacement, accumulated plastic strain and stress deviations of the multiscale problem with a elastoplastic RVE for different numbers of POD modes after unloading

	u_x	u_y	u_z	ε_{pl}		
$m = 6$	$2.1 \cdot 10^{-1}$	$2.2 \cdot 10^{-1}$	289	$1.1 \cdot 10^{-1}$		
$m = 12$	$3.0 \cdot 10^{-2}$	$1.4 \cdot 10^{-2}$	13.14	$2.3 \cdot 10^{-2}$		
$m = 24$	$3.0 \cdot 10^{-2}$	$3.8 \cdot 10^{-2}$	18.23	$2.7 \cdot 10^{-2}$		
	σ_{xx}	σ_{yy}	σ_{zz}	σ_{xy}	σ_{xz}	σ_{yz}
$m = 6$	$7.6 \cdot 10^{-2}$	$2.1 \cdot 10^{-1}$	$2.8 \cdot 10^{-2}$	$6.2 \cdot 10^{-2}$	43	1.99
$m = 12$	$7.0 \cdot 10^{-3}$	$5.1 \cdot 10^{-2}$	$3.8 \cdot 10^{-2}$	$2.2 \cdot 10^{-2}$	5.6	0.165
$m = 24$	$1.0 \cdot 10^{-2}$	$3.9 \cdot 10^{-2}$	$3.9 \cdot 10^{-2}$	$2.5 \cdot 10^{-2}$	1.28	0.81

The table gives the maximum values of the relative deviation $|\Delta(*)|^* = |\overline{(*)} - (*)|/max(|(*)|)$ of each field $\overline{(*)}$ computed in the FEPOD computation in comparison with the corresponding field $(*)$ of the reference FE^2 computation for the multiscale example with elastoplastic material behavior and a different number of POD modes
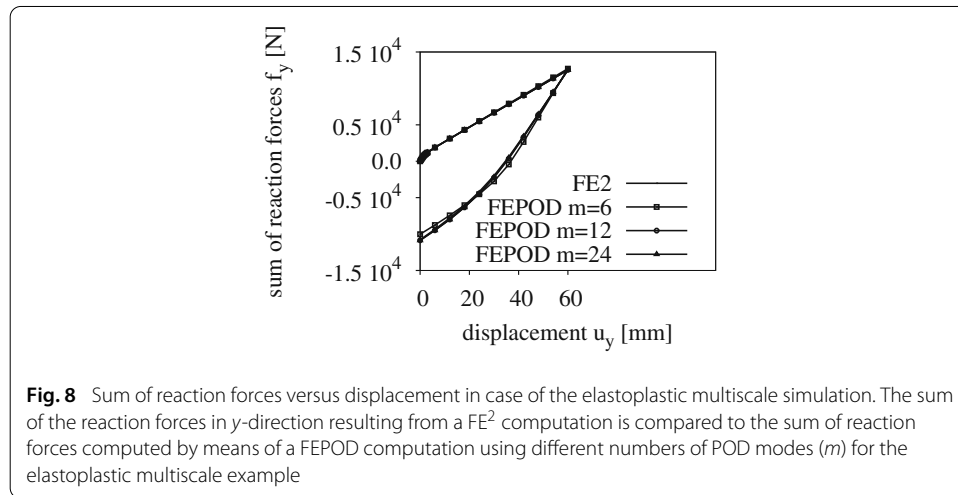
Fig. 8 Sum of reaction forces versus displacement in case of the elastoplastic multiscale simulation. The sum of the reaction forces in *y*-direction resulting from a FE^2 computation is compared to the sum of reaction forces computed by means of a FEPOD computation using different numbers of POD modes (*m*) for the elastoplastic multiscale example
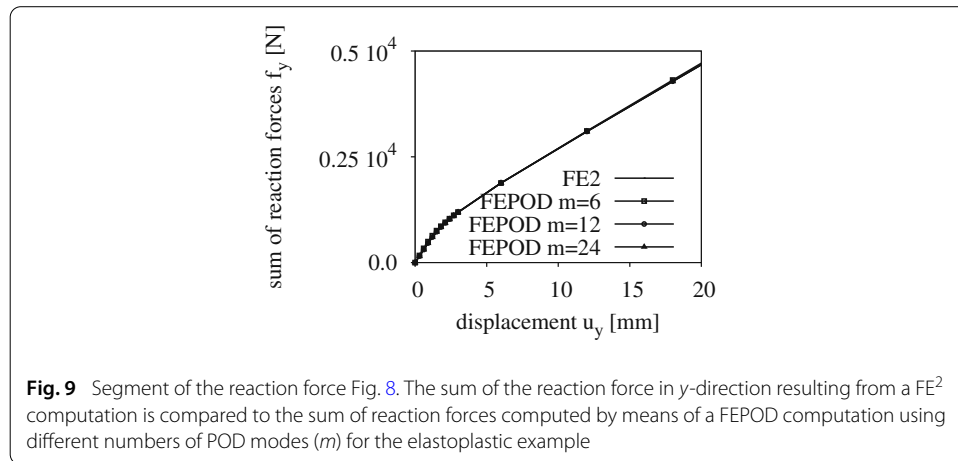
Fig. 9 Segment of the reaction force Fig. 8. The sum of the reaction force in *y*-direction resulting from a FE^2 computation is compared to the sum of reaction forces computed by means of a FEPOD computation using different numbers of POD modes (*m*) for the elastoplastic example

the overall behavior very precisely with a few POD modes at the micro scale. The loading and the unloading path are captured. The plot of the reaction force also shows that the deformation is accompanied by significant plastification of the structure. Of course, the example shows only linear hardening based on the used RVE.

To summarize, the second example of a metal matrix composite shows that the proposed FEPOD multiscale approach leads to good results with errors smaller 5% for the relevant

data and a high speed-up of around 180 ($m = 12$). Note also that working with the FEPOD approach does not significantly change the number of iterations per Newton step compared to the FE^2 approach. Similarly to the FE^2 approach, the FEPOD method shows quadratic convergence in the Newton iteration.

Hyperelastic material behavior

The derived FEPOD method is finally applied to a hyperelastic microstructure. In this example a simplified microstructure with four cubic material domains and 384 free degrees-of-freedom is investigated. Two of them contain a rather stiff material with a Young's modulus of 100 N/mm^2 and a Poisson's ratio of 0.3. The other two are filled with a soft material (Young's modulus equal to 1 N/mm^2, Poisson's ratio equal to 0.45).

In the case of large deformations, the POD subspace of the RVE is computed by means of precomputations of the nine independent deformation states. The microstructure is loaded separately by means of macroscopic deformation states where only one component is unequal to zero and increased until 1. For each of the nine precomputations 100 snapshots over loading time are collected. Based on the joined snapshot matrix, the POD subspace for the micro scale is computed. The decay of the normalized eigenvalues is shown in Fig. 10. The decay is similar to the previous example. After around 40 modes a further benefit by using more modes cannot be expected.

Again, the first investigation concerns the RVE. Figure 11 shows the approximation error (Eq. (28)) in the macroscopic stress response (Cauchy stresses) of the POD-reduced hyperelastic RVE using different numbers of POD modes. The RVE is arbitrarily loaded by the macroscopic deformation state

$$F_M = \begin{bmatrix} 1.0 & 0.2 & 0.6 \\ 0.0 & 0.2 & 0.5 \\ 0.0 & 0.7 & 0.0 \end{bmatrix}. \tag{30}$$

As expected, the error decreases with increasing number of POD modes. Using around 27 POD modes yield errors in the range of 10^{-3}, which promises good results in the reduced multiscale simulation.

Now the multiscale problem is studied by means of the hyperelastic RVE. A different macrostructure is investigated to take the hyperelastic behavior into account. For that pur-
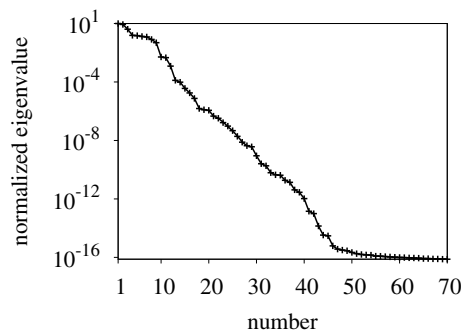
Fig. 10 Decay of the normalized eigenvalues in case of the hyperelastic matrix composite. The normalized eigenvalues of the correlation matrix based on the snapshots of the nine independent deformation states of the hyperelastic RVE decrease rapidly

Radermacher *et al. Adv. Model. and Simul. in Eng. Sci.*(2016)3:29

Page 19 of 23
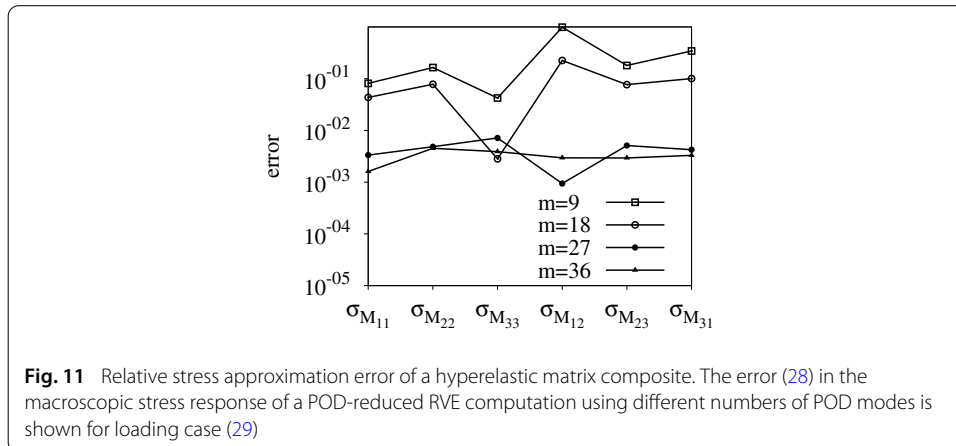
Fig. 11 Relative stress approximation error of a hyperelastic matrix composite. The error (28) in the macroscopic stress response of a POD-reduced RVE computation using different numbers of POD modes is shown for loading case (29)

pose, a cube under tension shown in Fig. 12 is created. As a consequence of symmetry only one quarter of the whole cube is simulated. The dimensions of the quarter are 100 mm × 100 mm × 100 mm leading to 1800 unknown degrees-of-freedom. Symmetry conditions are used on the planes $x_1 = 0$ and $x_2 = 0$. On the bottom the system is fixed in x_3-direction. The nodes on the top are constrained in x_1- and x_2-direction. The tension load is applied linear in time on one quarter of the top plane (black area in the Fig. 12). The system is discretized by $8 \times 8 \times 8$ elements. As a first test a FEPOD simulation with nine POD modes is compared to a full multiscale FE^2 simulation. In a study of convergence, it was checked that nine POD modes are sufficient to yield a result which is very close to the result of the FE^2 method. With this basis a very good approximation of the reference results can be reached. The relative displacement error in x_3-direction as well as the most relevant stress error are shown in Table 5 over the simulation time. The errors increase with increasing time because the degree of nonlinearity increases. In total, a very good approximation with errors smaller than 7% are reached. The comparison of the FEPOD results and the ones of FE^2 are summarized in Fig. 13. Of course, more investigations shall be carried out in the future. These will concern the dependence of the results on e. g. the number of chosen POD modes and the choice of the precomputations (inclusion of mixed deformation states).
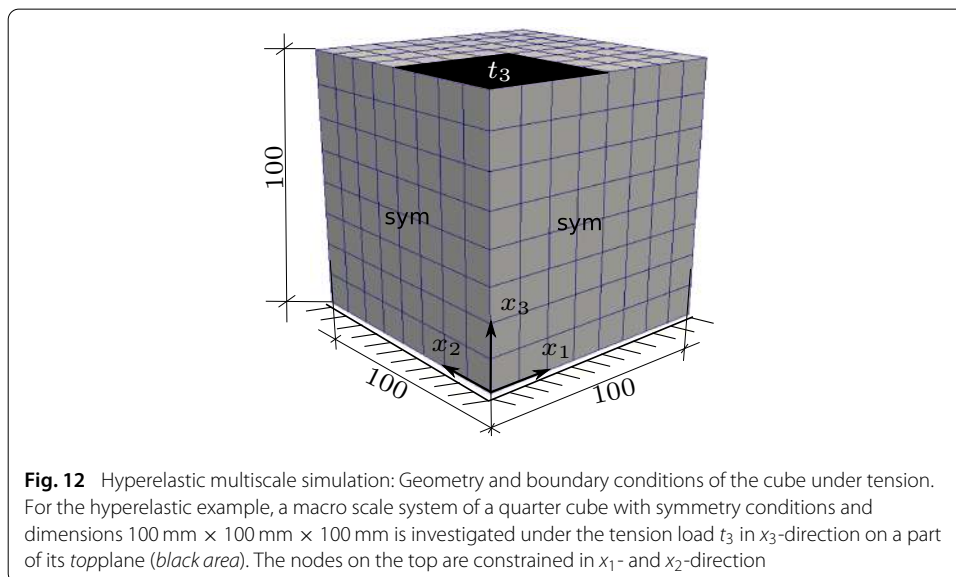
Fig. 12 Hyperelastic multiscale simulation: Geometry and boundary conditions of the cube under tension. For the hyperelastic example, a macro scale system of a quarter cube with symmetry conditions and dimensions 100 mm × 100 mm × 100 mm is investigated under the tension load t_3 in x_3-direction on a part of its *top*plane (*black area*). The nodes on the top are constrained in x_1- and x_2-direction

Table 5 Relative displacement and relative stress error of the multiscale problem with a hyperelastic RVE

t	u_3	σ_{33}
1000	0.000	0.000
2000	0.000	0.008
3000	0.009	0.010
4000	0.028	0.024
5000	0.048	0.045
6000	0.071	0.064

The table gives the error values over time of the relative deviation $|\Delta(*)|^* = |\overline{(*)} - (*)|/(|(*)|)$ of the displacement component $\overline{u_3}$ and stress field $\overline{\sigma}_{33}$ computed in the FEPOD computation in comparison with the corresponding values $(*)$ of the reference FE^2 computation for the multiscale example with hyperelastic material behavior
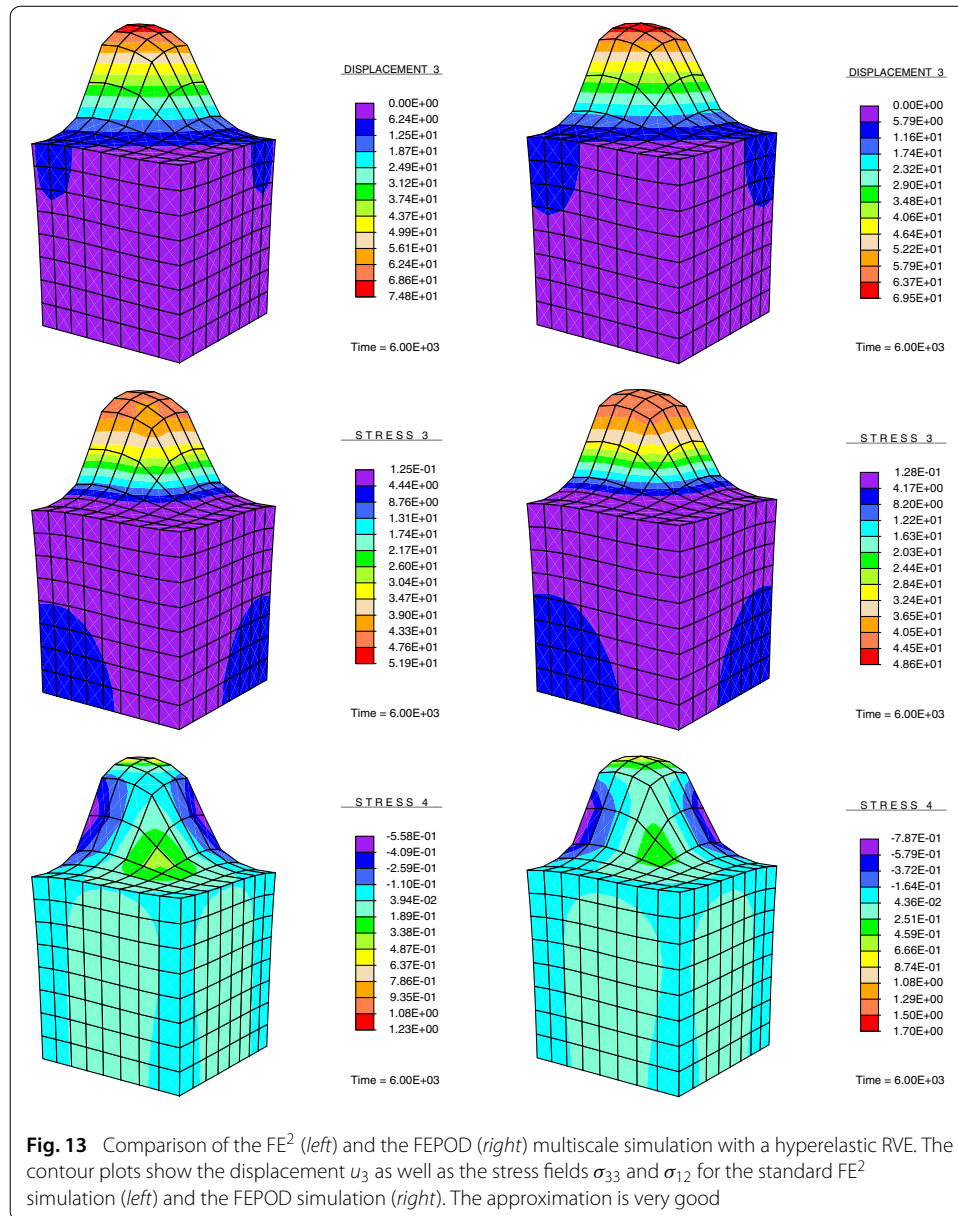
Fig. 13 Comparison of the FE^2 (*left*) and the FEPOD (*right*) multiscale simulation with a hyperelastic RVE. The contour plots show the displacement u_3 as well as the stress fields σ_{33} and σ_{12} for the standard FE^2 simulation (*left*) and the FEPOD simulation (*right*). The approximation is very good

Radermacher *et al. Adv. Model. and Simul. in Eng. Sci.(2016)3:29*

Page 21 of 23

Conclusions

This paper presents a new multiscale concept FEPOD where a reduced RVE computation is embedded into a finite element-based macro-mechanical simulation. Therefore, the POD reduction is carried out for the micro-mechanical boundary value problem. After this offline step, the RVE is represented by only a few POD modes. In this way it is possible to decrease the computational demands of a multiscale simulation enormously. Furthermore, the consistent macroscopic tangent for the FEPOD has been derived.

In case of a linear elastic composite, the FEPOD approach with only six POD modes leads to the same accuracy as a classical FE^2 approach. This is due to the principle of superposition which holds for linear elasticity. In case of plasticity, a few more POD modes are necessary to reach good accuracy. It is shown that also unloading phases are approximated in a very good way. In the investigated examples, speed-ups of around 250 times are possible while maintaining a high level of accuracy with errors less than 1% on the micro scale and less than 5% on the macro scale. Furthermore, a first test example concerning hyperelastic RVEs is shown. The example shows the successful application of FEPOD to large deformation. Of course, this topic has to be investigated in more detail in further research.

The computation of the reduced modes in the offline step is one important part of the proposed FEPOD approach, because the quality of the computed subspace significantly influence the accuracy of the reduced computation. In that offline step, the RVE has to be solved at least for the independent deformation states. This set-up was shown in the examples. In some cases, more than the six or nine independent deformation states have to be precomputed. This holds in particular for the case of highly nonlinear behavior where it is not possible to work with the assumption of superposition. It will be addressed in further investigations which states are most useful and how these states can be chosen. Also updating strategies of the modes on the fly during a FEPOD simulation should be further explored.

In summary, the proposed FEPOD method is able to increase the computational efficiency of a finite element based multiscale simulation significantly while maintaining a high level of accuracy. Therefore it is a promising approach for future research in multiscale modeling of not only fiber-reinforced composites but also other heterogeneous materials.

Author details
[1]Institute of Applied Mechanics, Mies-van-der-Rohe-Str. 1, 52074 Aachen, Germany, [2]Materials and Structures Division, NASA Glenn Research Center, 21000 Brookpark Rd., Cleveland, OH 44135, USA.

Competing interests
The authors declare that they have no competing interests.

References
1. Feyel F, Chaboche J-L. Fe2 multiscale approach for modelling the elastoviscoplastic behaviour of long fibre sic/ti composite materials. Comput Methods Appl Mech Eng. 2000;183(3–4):309–30. doi:10.1016/S0045-7825(99)00224-8.

Radermacher *et al. Adv. Model. and Simul. in Eng. Sci.(2016)3:29*

Page 22 of 23

2. Geers MGD, Kouznetsova VG, Brekelmans WAM. Multi-scale computational homogenization: trends and challenges. J Comput Appl Math. 2010;234(7):2175–82. doi:10.1016/j.cam.2009.08.077. Fourth International Conference on Advanced Computational Methods in Engineering (ACOMEN 2008).
3. Ladevèze P, Loiseau O, Dureisseix D. A micro-macro and parallel computational strategy for highly heterogeneous structures. Int J Numer Methods Eng. 2001;52(1–2):121–38. doi:10.1002/nme.274.
4. Ladevèze P, Nouy A. On a multiscale computational strategy with time and space homogenization for structural mechanics. Comput Methods Appl Mech Eng. 2003;192(28–30):3061–87. Multiscale Computational Mechanics for Materials and Structures.
5. Aboudi J. Micromechanical analysis of thermo-inelastic multiphase short-fiber composites. Compos Eng. 1995;5:839–50.
6. Aboudi J, Arnold SM, Bednarcyk BA. Micromechanics of composite materials: a unified multiscale analysis approach. Amsterdam: Elsevier; 2013.
7. Michel JC, Suquet P. Computational analysis of nonlinear composite structures using the nonuniform transformation field analysis. Comput Methods Appl Mech Eng. 2004;193(48–51):5477–502. doi:10.1016/j.cma.2003.12.071. Advances in Computational Plasticity.
8. Michel JC, Suquet P. Nonuniform transformation field analysis. Int J Solids Struct. 2003;40(25):6937–55. doi:10.1016/S0020-7683(03)00346-9 (Special issue in Honor of George J. Dvorak).
9. Dvorak GJ, Benveniste Y. On transformation strains and uniform fields in multiphase elastic media. The Royal Society; 1992. pp. 291–310.
10. Fritzen F, Böhlke T. Reduced basis homogenization of viscoelastic composites. Compos Sci Technol. 2013;76:84–91. doi:10.1016/j.compscitech.2012.12.012.
11. Fritzen F, Leuschner M. Reduced basis hybrid computational homogenization based on a mixed incremental formulation. Comput Methods Appl Mech Eng. 2013;260:143–54. doi:10.1016/j.cma.2013.03.007.
12. Fritzen F, Hodapp M, Leuschner M. GPU accelerated computational homogenization based on a variational approach in a reduced basis framework. Comput Methods Appl Mech Eng. 2014;278:186–217. doi:10.1016/j.cma.2014.05.006.
13. Largenton R, Michel J-C, Suquet P. Extension of the nonuniform transformation field analysis to linear viscoelastic composites in the presence of aging and swelling. Mech Mater. 2014;73:76–100. doi:10.1016/j.mechmat.2014.02.004.
14. Oskay C, Fish J. Eigendeformation-based reduced order homogenization for failure analysis of heterogeneous materials. Comput Methods Appl Mech Eng. 2007;196(7):1216–43. doi:10.1016/j.cma.2006.08.015.
15. Sparks P, Oskay C. Identification of optimal reduced order homogenization models for failure of heterogeneous materials. Int J Multiscale Comput Eng. 2013;11(3):185–200.
16. Chinesta F, Ammar A, Cueto E. Recent advances and new challenges in the use of the proper generalized decomposition for solving multidimensional models. Arch Comput Methods Eng. 2010;17:327–50. doi:10.1007/s11831-010-9049-y.
17. Ladevèze P, Passieux JC, Néron D. The multiscale computational method and the proper generalized decomposition. Comput Methods Appl Mech Eng. 2010;199(21—-22):1287–96.
18. Cremonesi M, Néron D, Guidault P-A, Ladevèze P. A pgd-based homogenization technique for the resolution of nonlinear multiscale problems. Comput Methods Appl Mech Eng. 2013;267:275–92. doi:10.1016/j.cma.2013.08.009.
19. El Halabi F, González D, Chico A, Doblaré M. Fe2 multiscale in linear elasticity based on parametrized microscale models using proper generalized decomposition. Comput Methods Appl Mech Eng. 2013;257:183–202. doi:10.1016/j.cma.2013.01.011.
20. Boyaval S. Reduced-basis approach for homogenization beyond the periodic setting. Multiscale Model Simul. 2008;7(1):466–94. doi:10.1137/070688791.
21. Kerfriden P, Ródenas JJ, Bordas SP-A. Certification of projection-based reduced order modelling in computational homogenisation by the constitutive relation error. Int J Numer Methods Eng. 2014;97(6):395–422. doi:10.1002/nme.4588.
22. Hesthaven JS, Zhang S, Zhu X. Reduced basis multiscale finite element methods for elliptic problems. Multiscale Model Simul. 2015;13(1):316–37. doi:10.1137/140955070.
23. Abdulle A, Bai Y. Adaptive reduced basis finite element heterogeneous multiscale method. Comput Methods Appl Mech Eng. 2013;257:203–20. doi:10.1016/j.cma.2013.01.002.
24. Goury O, Kerfriden P, Bordas S. Bridging analytical and computational homogenisation for nonlinear multiscale problems: a reduced order modelling approach for a damage problem. Technical report; 2014. https://hal.archives-ouvertes.fr/hal-00994923
25. Miled B, Ryckelynck D, Cantournet S. A priori hyper-reduction method for coupled viscoelastic-viscoplastic composites. Comput Struct. 2013;119:95–103. doi:10.1016/j.compstruc.2012.11.017.
26. Ryckelynck D. A priori hyperreduction method: an adaptive approach. J Comput Phys. 2005;202(1):346–66. doi:10.1016/j.jcp.2004.07.015.
27. Hernández JA, Oliver J, Huespe AE, Caicedo MA, Cante JC. High-performance model reduction techniques in computational multiscale homogenization. Comput Methods Appl Mech Eng. 2014;276:149–89. doi:10.1016/j.cma.2014.03.011.
28. Monteiro E, Yvonnet J, He QC. Computational homogenization for nonlinear conduction in heterogeneous materials using model reduction. Comput Mater Sci. 2008;42(4):704–12. doi:10.1016/j.commatsci.2007.11.001.
29. Yvonnet J, He Q-C. The reduced model multiscale method (r3m) for the non-linear homogenization of hyperelastic media at finite strains. J Comput Phys. 2007;223(1):341–68. doi:10.1016/j.jcp.2006.09.019.
30. Xia L, Breitkopf P. A reduced multiscale model for nonlinear structural topology optimization. Comput Methods Appl Mech Eng. 2014;280:117–34. doi:10.1016/j.cma.2014.07.024.
31. Taylor RL. Feap—a finite element analysis program, Version 8.3 User manual. University of California at Berkeley; 2011. www.ce.berkeley.edu/projects/feap. Accessed 05 Apr 2011.
32. Feyel F. Multiscale FE2 elastoviscoplastic analysis of composite structures. Comput Mater Sci. 1999;16(1–4):344–54. doi:10.1016/S0927-0256(99)00077-4.

33. Kouznetsova VG. Computational homogenization for the multi-scale analysis of multi-phase materials. PhD thesis, Technische Universiteit Eindhoven; 2002.
34. Miehe C, Koch A. Computational micro-to-macro transitions of discretized microstructures undergoing small strains. Arch Appl Mech. 2002;72(4):300–17. doi:10.1007/s00419-002-0212-2.
35. Kanit T, Forest S, Galliet I, Mounoury V, Jeulin D. Determination of the size of the representative volume element for random composites: statistical and numerical approach. Int J Solids Struct. 2003;40(13–14):3647–79. doi:10.1016/S0020-7683(03)00143-4.
36. van der Sluis O, Schreurs PJG, Brekelmans WAM, Meijer HEH. Overall behaviour of heterogeneous elastoviscoplastic materials: effect of microstructural modelling. Mechan Mater. 2000;32(8):449–62.
37. Terada K, Hori M, Kyoya T, Kikuchi N. Simulation of the multi-scale convergence in computational homogenization approach. Int J Solids Struct. 2000;37(16):2285–311.
38. Kouznetsova V, Brekelmans WAM, Baaijens FPT. An approach to micro-macro modeling of heterogeneous materials. Comput Mech. 2001;27:37–48.
39. Reese S, Wriggers P. A finite element method for stability problems in finite elasticity. Int J Numer Methods Eng. 1995;38(7):1171–200.
40. Breuer KS, Sirovich L. The use of the karhunen-loéve procedure for the calculation of linear eigenfunctions. J Comput Phys. 1991;96(2):277–96. doi:10.1016/0021-9991(91)90237-F.
41. Sirovich L. Chaotic dynamics of coherent structures. Phys D Nonlinear Phenom. 1989;37(1–3):126–45. doi:10.1016/0167-2789(89)90123-1.
42. Radermacher A, Reese S. A comparison of projection-based model reduction concepts in the context of nonlinear biomechanics. Arch Appl Mech. 2013;83(8):1193–213. doi:10.1007/s00419-013-0742-9.
43. Radermacher A, Reese S. Proper orthogonal decomposition-based model reduction for non-linear biomechanical analysis. Int J Mater Eng Innov. 2013;4(2):149–65. doi:10.1504/IJMATEI.2013.054393.
44. Astrid P, Weiland S, Willcox K, Backx T. Missing point estimation in models described by proper orthogonal decomposition. IEEE Trans Autom Control. 2008;53:2237–51. doi:10.1109/TAC.2008.2006102.
45. Chaturantabut S, Sorensen DC. Nonlinear model reduction via discrete empirical interpolation. SIAM J Sci Comput. 2010;32(5):2737–64. doi:10.1137/090766498.
46. Grepl MA. Model order reduction of parametrized nonlinear reaction-diffusion systems. Comput Chem Eng. 2012;43:33–44. doi:10.1016/j.compchemeng.2012.03.013.
47. Nguyen NC, Patera AT, Peraire J. A 'best points' interpolation method for efficient approximation of parametrized functions. Int J Numer Methods Eng. 2008;73(4):521–43. doi:10.1002/nme.2086.
48. Carlberg K, Bou-Mosleh C, Farhat C. Efficient non-linear model reduction via a least-squares Petrov–Galerkin projection and compressive tensor approximations. Int J Numer Methods Eng. 2011;86(2):155–81. doi:10.1002/nme.3050.
49. Farhat C, Avery P, Chapman T, Cortial J. Dimensional reduction of nonlinear finite element dynamic models with finite rotations and energy-based mesh sampling and weighting for computational efficiency. Int J Numer Methods Eng. 2014;98(9):625–62. doi:10.1002/nme.4668.
50. Stier B, Bednarcyk BA, Simon JW, Reese S. Investigation of micro-scale architectural effects on damage of composites. NASA/TM–2015-218740; National Technical Information Service; 2015.
51. Stier B, Simon JW, Reese S. Numerical and experimental investigation of the structural behavior of a carbon fiber reinforced ankle-foot orthosis. Med Eng Phys. 2015;37:505–11.